Fabrication-Tolerant O-Band WDM Filter With Phase-Balanced Tapered Arms and Wavelength-Independent Couplers

Marios Papadovasilakis , Sujith Chandran , Yonas Gebregiorgis , Yusheng Bian , Michal Rakowski, Abdelsalam Aboketaf , Rod Augur, and Jaime Viegas , *Member, IEEE*

Abstract—We design, simulate, and experimentally demonstrate a coarse wavelength-division de-multiplexing system based on cascaded Mach-Zehnder interferometers (MZIs) operating in the O-band. The fabricated devices are built on a monolithic silicon photonics platform in a state-of-the-art CMOS foundry. The fabrication tolerance of the device was obtained by a combination of analytical and 3D Finite-difference time-domain (FDTD) methods. Fabrication-tolerant wavelength-independent couplers were used in order to achieve broadband splitting ratios (SRs) and ensure device stability along the entire wavelength range. In addition, phase-balanced linear tapers were used to allow for arbitrary waveguide width values for the MZIs. Experimental results show very high-performance stability across different wafer test sites with a mean channel spectral shift of only 1.03 nm and a total device footprint of 0.582 mm^2.

Index Terms—Mach-Zehnder interferometer, WDM, wavelength-independent coupler, fabrication-tolerant, silicon photonics.

I. INTRODUCTION

WAVELENGTH Division Multiplexing (WDM) is a widely used robust technique to increase the channel bandwidth of photonic integrated circuits (PICs). A large number of independent signals can be transmitted simultaneously as different wavelengths propagate along a single waveguide. Various techniques have been suggested in the literature for WDM applications. One common technique is ring resonator-based WDM filters [1], [2], [3]. These devices are very compact, although due to their resonant nature they are very prone to fabrication errors or temperature variations. Another type of

filters are arrayed waveguide gratings (AWGs) [4], [5], [6] or Echelle gratings [7], [8], [9]. Conventional AWG structures use power splitters based on wavefront division using free propagation regions (FPRs). The shortcomings of these power splitters are higher insertion loss, non-uniform power splitting, stringent fabrication requirements, and large device footprint. More recently, WDM devices based on contra-directional coupling using sub-wavelength gratings [10], [11], [12], [13], [14] have been proposed. SWG-based devices demonstrate flat-top filter response, which enables them to exhibit robust performance. Lastly, another type of WDM design is realized by cascading Mach-Zehnder Interferometers and organizing them in distinct stages with precisely tuned power coupling coefficients [15], [16], [17], [18]. For a silicon-on-insulator (SOI) platform, the high index contrast between the waveguide core and cladding enables strong mode confinement and a compact device footprint. Precise device fabrication is crucial, as inevitable fabrication errors have an adverse effect on the device performance [19]. Additionally, silicon has a high thermo-optic coefficient [20] which emphasizes the importance of temperature stability. MZI-based designs offer a particularly attractive solution, as MZIs have been shown to demonstrate fabrication-tolerant [21] and athermal [22], [23], [24] performance. Thus, suitably designed MZIs can be used to demonstrate a passive flat-top cWDM filter without introducing any active elements (e.g., heaters [25]) to compensate for fabrication and/or thermal variation. However, most fabrication-tolerant MZI-based WDM systems, utilize standard directional couplers (DCs) to achieve the necessary power splitting ratios (SRs) [26], [27]. The principle of operation of a DC relies on evanescent field interaction between two waveguides that are placed in parallel and spaced by a short gap. Their operation can be described by coupled mode theory [28], [29]. Typically, DCs have a small footprint and exhibit low insertion loss (IL). However, the power SR of a DC suffers from strong wavelength dependence [30], which can make them an unsuitable choice for broadband applications, such as WDM systems. MZI-based WDM devices rely on precisely tuned splitting ratios between subsequent MZIs, thus the wavelength-dependent nature of DCs would result in imperfect MZI interference conditions for channels spectrally located far from the wavelength range center. One particular study [18] used bent DCs, which can constrain the strong wavelength dependency of the SR. However, this study does not investigate the demonstration of fabrication

tolerant performance. Other types of wavelength-independent power splitters exist in the literature, nevertheless, they have not yet been implemented in WDM configurations. In this paper, we demonstrate broadband, fabrication-tolerant, MZI-based, coarse WDM filters with wavelength-independent couplers (WICs) and phase-balanced tapered arms, that are fabricated on a monolithic silicon photonics platform.

The inclusion of WICs helps us achieve broadband operation throughout the O-band, without compromising the characteristics of channels located on either side of the spectrum. We first perform a rigorous analysis of the WIC design. We present a robust semi-analytical approach that guarantees consistent WIC performance across different wafer sites. The model is tested through experimental measurements, where we implement an intentional waveguide width offset to successfully verify the device's tolerance to typical fabrication variations. Having secured robust WIC performance, we next aim for fabrication-tolerant MZIs. We use optimized MZI arm widths, which enable fabrication-insensitive performance through the implementation of phase-balanced linear tapers. We fabricate two different WDM configurations, which allows us to quantify the trade-off between device footprint and fabrication robustness. Both filters demonstrate excellent fabrication stability with a mean channel maximum spectral shift of 1.03 nm and 2.45 nm. However, the device crosstalk is affected by an imperfectly tuned 3-dB power splitter, albeit with consistent performance across different wafer dies. Using adiabatic Bézier bends can help minimize the IL and stabilize the SR further [31], while also reducing the total device footprint. Moreover, the proposed de-multiplexers are demonstrated on a monolithic CMOS-compatible SOI platform with a thin (160 nm) device layer [32]. This allows for seamless integration of the filters with state-of-the-art CMOS electronics and silicon nitride photonic components on the same chip [33], [34], [35], [36], [37]. This paper is structured as follows. We first present the design strategy behind the wavelength-independent couplers, followed by the design of the fabrication-tolerant MZIs. Subsequently, we combine these two structures to generate the cWDM filter, and finally, the experimental results of two filter variations are presented.

II. DEVICE DESIGN AND SIMULATION

Successful operation of this WDM device mainly relies on two essential components; (i) the WIC which ensures wavelength-independent SRs over the entire wavelength of operation range, and (ii) the fabrication-tolerant MZIs which enable stable performance across different wafer sites. In this section, we will first examine each component individually where the theoretical background and simulation results will be presented.

A. Wavelength Independent Coupler

The WIC essentially consists of two DCs of different lengths L_{DC_1}, and L_{DC_2} separated by a delay section consisting of asymmetric arms of length difference ΔL as described theoretically in [38]. Fig. 1(a) shows an isometric view of a DC of length L_{DC}. Assuming that the structure exhibits zero IL and $|E_{in}|^2 = P_{in} = 1$, the magnitude of the cross-coupled electric
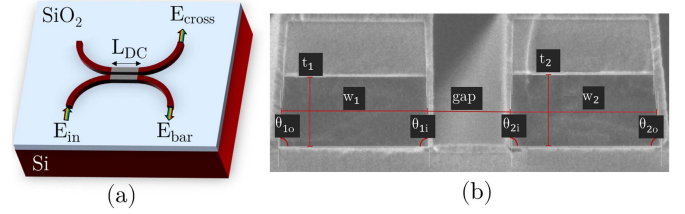

Fig. 1. (a) Schematic illustration of a DC; (b) SEM Cross-section image of the fabricated DC depicting the fabricated geometrical features, i.e., w, t, and θ, which represent the waveguide width, thickness, and sidewall angles, respectively.
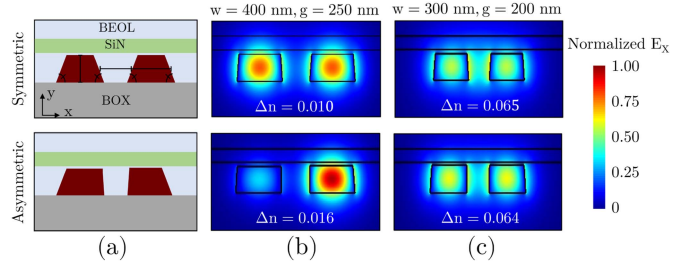

Fig. 2. Modal analysis of various DC cross-sections. (a) Cross-section illustration of the symmetric and asymmetric DC [39]; Electric field distribution of the fundamental TE mode of a DC for a symmetric (top row) and asymmetric (bottom row) geometry for (b) a cross-section of 400 nm width, and 250 nm gap, and (c) a cross-section of 300 nm width, and 200 nm gap. The term BEOL refers to the back-end-of-the-line.

field $|E_{cross}|$ will be equal to the field coupling coefficient κ as [28], [29]:

$$|E_{cross}| = \kappa = \sin\left(\frac{\pi \Delta n}{\lambda} L_{DC} + \theta_0\right), \quad (1)$$

where λ is the wavelength, Δn is the effective index difference between the symmetric and anti-symmetric modes of the coupler, and θ_0 is a phase term that corresponds to the coupling induced by the bent waveguides located on either side of the straight waveguides. Henceforth, we will denote the SR as $SR = P_{cross} = |\kappa|^2$.

Equation (1) is sufficient to calculate the coupled electric field from a DC, however, this analytical expression only applies for symmetric waveguides, i.e. waveguides that consist of identical critical parameters such as width, thickness, and sidewall angles. Fig. 1(b) shows a scanning electron microscope (SEM) image of a cross-section of a directional coupler, with intended waveguide width of 400 nm for both waveguides. It is apparent that all three critical parameters of the waveguides demonstrate deviation from the intended values. Thus, the two waveguides are not geometrically symmetric, which means that (1), in principle, no longer applies. We can assess the effect of these geometrical deviations by comparing the spectral response of a directional coupler obtained by (1) with 3D-FDTD simulations. The first step is calculating the term Δn using Lumerical's Finite Difference Eigenmode (FDE) solver. Fig. 2(a) shows a cross-section schematic for the case of a perfectly symmetric and an asymmetric DC. The asymmetric DC dimensions are directly implemented by the measured values as shown in the SEM image of Fig. 1(b). These cross-sections were used in order to obtain
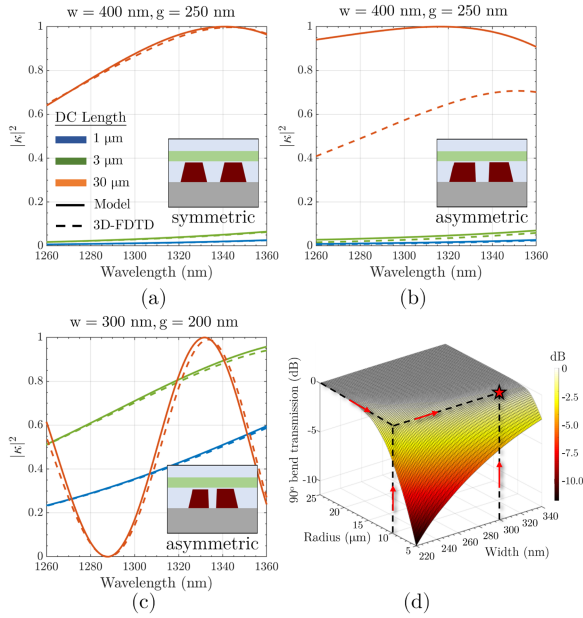
Fig. 3. Comparison of the SR between the semi-analytical model and 3D-FDTD simulations for DC lengths of 1, 3, and 30 μm for: (a) symmetric cross-section of 400 nm width, and 250 nm gap, (b) asymmetric cross-section of 400 nm width, and 250 nm gap, and (c) asymmetric cross-section of 300 nm width, and 200 nm gap. Inset schematics illustrate the respective cross-section of each DC. (d) Surface plot of the transmitted power across a 90° bend for various waveguide widths and bend radii. The red star symbol corresponds to the chosen set of parameters aiming at a trade-off between minimizing the width and radius while maintaining high transmitted power.

the modal fields shown in Fig. 2(b) and (c), which show the fundamental mode for the case of the symmetric and asymmetric cross-section for a waveguide width of 400 and 300 nm and gap of 250 nm and 200 nm, respectively. In the symmetric case, we notice that the electric field is uniformly distributed between the two waveguides, as expected. Conversely, in the asymmetric case of the wider waveguides (Fig. 2(b)) the electric field is no longer distributed uniformly. Additionally, there is a large difference of 45.7% in Δn. In the case of the asymmetric narrow waveguides, however, we notice that the electric field retains its uniformity, and that difference in Δn is only 4.3%. This can be attributed to the fact that narrow waveguides enable higher modal delocalization from the waveguide core, thus the electric field interacts more strongly with the cladding, and more weakly with potential waveguide geometrical variations. Additionally, the short gap enables stronger evanescent coupling, which leads to shorter DC lengths, thus reducing the total device footprint. Moreover, as the DC length is increased, any potential fabrication-induced errors will significantly impact the device's performance as phase error is accumulated along the length of the DC [40]. We verify the aforementioned assumption by performing 3D-FDTD simulations for each DC cross-section. Fig. 3(a) shows the spectral response of each for 3 DC lengths for a symmetric cross-section. As expected, the two models are in full agreement regardless of DC length. However, in the case of asymmetric and wide waveguides (Fig. 3(b)), the two models' spectral responses increasingly deviate as the DC length is increased, which confirms our initial assumption. This

deviation is absent, however, in the case of asymmetric narrow waveguides (Fig. 3(c)), due to the electric field uniformity shown in Fig. 2(c). Consequently, the DCs are designed with closely spaced narrow waveguides which can help suppress any adverse effects originating from the inherent geometrical asymmetries of the coupler. Thus, we expect the designed WICs to demonstrate consistent performance even in the presence of inevitable fabrication variability across the silicon wafer. Additionally, [28] also presents an expression for the coupling coefficient of an asymmetric-section DC, however, it refers to consistent asymmetry which is retained throughout the DC length. In a realistic case, the asymmetry will not be consistent along the waveguide length due to sidewall roughness. Moreover, since the entire WDM structure extends for several millimeters, there is a possibility that the cross-section will change along the device length. This is why we opt for a waveguide width and DC gap that will induce coupling which will not be affected by these effects and will provide consistent performance similar to the symmetric case, regardless of potential cross-section changes throughout the device.

To conclude, regarding the specific choice of parameters, we aimed at minimizing the bend radius in order to minimize footprint, as well as minimize the width, to achieve maximum mode delocalization. However, a weakly confined mode will suffer increased loss due to radiative modes while propagating along a bent waveguide. Thus, there exists a trade-off between minimizing footprint and mode delocalization, and maintaining low bend-induced loss. Fig. 3(d) shows a surface plot of the transmitted power for various radii and waveguide widths. Based on the above considerations and the displayed results of this graph, we choose a width of 300 nm and a bend radius of 10 μm. Lastly, we opt for a short gap of 200 nm to enhance the evanescent coupling and minimize the required DC length to achieve the necessary power SRs. One parameter to consider is the effect of potential sidewall roughness on the fabricated devices. The electric field intensity of a TE mode at the silicon/oxide interface is larger for narrower waveguides [40], which can cause increased loss due to sidewall roughness. This is supported in [41], where it is suggested that wider waveguides exhibit lower loss due to sidewall roughness in the C-band. The effect of loss due to sidewall roughness on different waveguide widths is beyond the scope of this work, however, it would be a useful consideration in future configurations aiming to minimize insertion loss.

Having determined the optimal DC dimensions, we proceed with designing all the necessary WIC configurations. Fig. 4(a) shows an isometric view of the WIC, consisting of the 4 critical parameters L_{DC_1}, L_{DC_2}, ΔL_{WIC_1}, and ΔL_{WIC_2}, while Fig. 4(b) shows a simulated top view of the electric field for a WIC aiming for an SR of 0.5. Albeit the two DCs exhibit wavelength-dependent response, accurate tuning of the delay introduced by ΔL_{WIC_1} achieves stable spectral performance. When targeting a specific SR value, we set values for the first three parameters such that the mean value of P_{cross} with respect to wavelength is approximately equal to the desired SR and $\frac{\Delta P_{cross}(\lambda)}{\Delta \lambda} \simeq 0$ to ensure that the power remains constant over
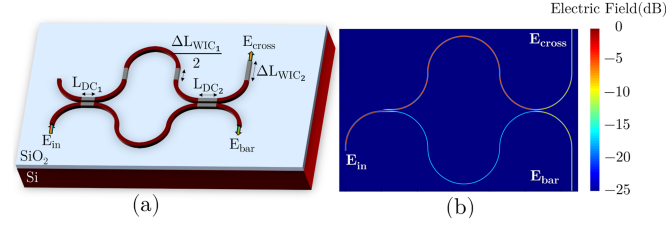
Fig. 4. Schematic illustration of a WIC consisting of two directional couplers of lengths L_{DC_1}, and L_{DC_2}, MZI of arm length separation ΔL_{WIC_1}, and phase compensation length of ΔL_{WIC_2}; (b) Top view of the electric field as obtained by 3D-FDTD simulation for a WIC aiming for a SR of 0.5.
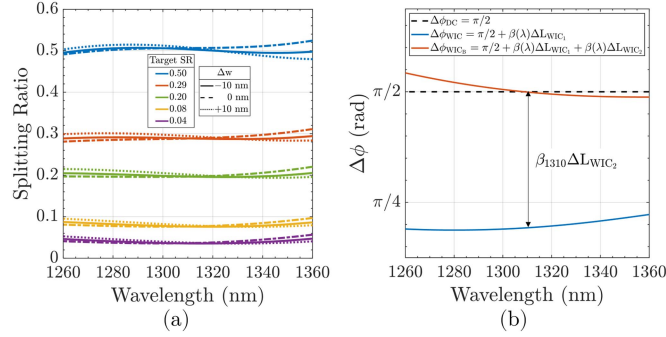

Fig. 5. Simulation results of the proposed WIC: (a) WIC power spectra for aiming at the different SRs dictated by [16]. Each WIC was simulated for a waveguide width offset of ± 10 nm to demonstrate the fabrication-tolerant behavior of the device; and (b) phase difference between the two arms at the output of a 50:50 DC (dashed), a 50:50 WIC (blue), and a 50:50 WIC with phase-balancing length (orange) included.

the O-band. The final parameter ΔL_{WIC_2} is used to adjust the phase difference between the cross and bar ports and will be explored subsequently. Fig. 5(a) shows the obtained spectra of the 5 different necessary SRs required for the successful operation of the WDM according to [16], [42]. The simulation results show a maximum offset of less than 1.5% from the desired SR for a waveguide width variation of ± 10 nm.

Achieving the necessary power ratios is not sufficient by itself. Standard 50:50 DCs with power entering only from one of the DC arms induce a fixed phase difference of $|\Delta\phi| = \pi/2$ between cross and bar ports for every wavelength [43]. The design rules dictating the lengths of the MZIs in [16] are based on SRs provided by DCs, however, a WIC contains 2 DCs and a delay length of ΔL_{WIC_1} on one of the arms, meaning that each WIC will induce a different $\Delta\phi$ which will depend on ΔL_{WIC_1}. Additionally, due to the inclusion of ΔL_{WIC_1}, the phase difference will be dispersive, i.e. $\Delta\phi$ will not be equal for all wavelengths. We compensate for this offset by introducing an additional length at the cross port of the WIC. It is noted that the phase-compensation length is based on the central wavelength of $\lambda = 1310$ nm, thus due to dispersion, the phase difference will not be constant over the O-band. A waveguide width offset on a ΔL_{WIC_2} segment could potentially induce a phase shift that would affect the output spectrum. For this reason, the fabricated devices contain these ΔL_{WIC_1} lengths within the $w_{H/L}$ segments of each MZI (see Section II-B), including them in the overall length set by the condition for fabrication tolerant operation. Thus, any potential

TABLE I
GEOMETRICAL PARAMETERS OF EACH WIC FOR VARIOUS SPLITTING RATIOS

SR	L_{DC_1}/L_0	L_{DC_2}/L_0	$\Delta L_{WIC_1}/L_0$
0.50	1.12	0	0.18
0.29	0.81	0	0.16
0.20	0.72	0.02	0.14
0.08	0.54	0	0.13
0.04	0.48	0.02	0.13

The lengths are normalized with respect to the DC cross-over length L_0 [43], i.e., the length required for a full power transfer between the two waveguides.

width deviation of these lengths will not affect the performance of the WDM. The electric field at the output of the WIC (2) is defined by cascading the matrix elements of each individual component, i.e. the directional couplers and delay lines:

$$
\begin{bmatrix} E_{\text{cross}} \\ E_{\text{bar}} \end{bmatrix} = \underbrace{\begin{bmatrix} e^{i\beta_2 \Delta L_{WIC_2}} & 0 \\ 0 & 1 \end{bmatrix}}_{\Delta L_{WIC_2}} \underbrace{\begin{bmatrix} t_2 & i\kappa_2 \\ i\kappa_2 & t_2 \end{bmatrix}}_{DC_2} \underbrace{\begin{bmatrix} e^{i\beta_1 \Delta L_{WIC_1}} & 0 \\ 0 & 1 \end{bmatrix}}_{\Delta L_{WIC_1}}
$$
$$
\underbrace{\begin{bmatrix} t_1 & i\kappa_1 \\ i\kappa_1 & t_1 \end{bmatrix}}_{DC_1} \begin{bmatrix} 0 \\ E_{\text{in}}, \end{bmatrix} \tag{2}
$$

where, $t = \sqrt{1-\kappa^2}$, and $\beta_i = 2\pi n_{\text{eff},i}/\lambda$ is the propagation constant of each arm. The length of the delay line ΔL_{WIC_2} is defined such that:

$$
\angle E_{\text{cross}} - \angle E_{\text{bar}} = \pi/2 + \beta_1(\lambda)\Delta L_{WIC_1} + \beta_2(\lambda)\Delta L_{WIC_2}
$$
$$
\simeq m\pi/2, \tag{3}
$$

where m is an odd integer. Fig. 5(b) shows the induced phase difference between the cross and bar port for the WIC depicted in Fig. 1(b), and how the additional length ΔL_{WIC_2} compensates for the phase offset, induced by the MZI. It is important to note that the above discussion is considered for a 50:50 power splitter with power entering from one of the input arms. For different SRs and power ratios entering the DC, the phase difference between the propagating pulses of the output arms can be different than $\pi/2$. However, we can generalize the approach described above to any kind of splitting ratio or phase difference by adjusting the length of the term ΔL_{WIC_2}, such that the transfer function of the WIC will mimic the one obtained by a standard DC. Table I shows the parameters we used for each designed WIC.

B. Mach-Zehnder Interferometer

Having secured broadband SRs from the WIC, we will now present the design strategy behind the fabrication-tolerant MZIs. The phase condition for constructive interference of an MZI can be expressed as $\beta_1 L_1 - \beta_2 L_2 = 2m\pi$, where m is an integer and β_i, and L_i are the propagation constant and length of each arm, respectively. The sensitivity of an MZI to fabrication errors can be investigated by examining the spectral shift with respect

TABLE II
COMPARATIVE ANALYSIS OF THE RELEVANT FIGURES OF MERIT, I.E., MEAN
SPECTRAL SHIFT ($\overline{\Delta\lambda}$), INSERTION LOSS ($\overline{\text{IL}}$), CROSSTALK ($\overline{\text{XT}}$), AND
FOOTPRINT BETWEEN THIS WORK AND THE STATE-OF-THE-ART ON
SECOND-ORDER MZI-BASED WDM FILTERS

$\overline{\Delta\lambda}$ (nm)	$\overline{\text{IL}}$ (dB)	$\overline{\text{XT}}$ (dB)	Size (mm^2)	Reference
1.70	2.0	-24.0	0.18	[26]
0.67	2.3	-23.5	1.46	[27]
10.57	3.7	-19.8	1.91	[48]
1.66	5.8	-20.8	1.69	[49]
1.03	3.8	-22.1	0.58	This work

to waveguide width for the central wavelength λ_0 as in [23]:

$$\frac{\partial n_1}{\partial w} L_1 = \frac{\partial n_2}{\partial w} L_2 \tag{4a}$$

$$\text{FSR} = \frac{\lambda_0^2}{n_{g,1} L_1 - n_{g,2} L_2}, \tag{4b}$$

where n, n_g and L are the effective index, group index, and arm length, respectively. Equation (4) dictate the lengths and widths of each MZI arm to obtain fabrication-tolerant condition and the free spectral range (FSR) specification. A technique which was used in [27] sets the width of the first arm (w_L) equal to the width used in the DCs (w_0), while the width of the second arm w_H is defined arbitrarily. Subsequently, by defining the proper FSR, the arms' lengths are obtained through (4). The tapers which are used for the transition from w_L to w_H in the second arm are also added in the first arm in order to eliminate the excess phase-shift from the interference condition that is induced by the tapers.

This method merely allows the control of one of the arm's widths. However, it is useful to be able to control both widths because larger widths are less sensitive to width variations due to stronger mode confinement as can be seen in Fig. 6(a). Additionally, it was observed that larger widths exhibit a gradual slope with respect to wavelength, indicating that the effective index change will be lower and more uniform as compared to smaller widths. Choosing large widths allows us to include the bends to be the part of phase delay section ΔL, thus reducing the number of tapers from 4 to 2, which also leads to footprint reduction. Using w_L and w_H which are different from w_0 requires the inclusion of different tapers for each arm, specifically $w_0 \to w_L$ and $w_0 \to w_H$. The total phase difference between the two arms will now be:

$$\Delta\phi_{\text{tot}} = \underbrace{(\beta_1 L_1 - \beta_2 L_2)}_{\text{waveguides}} + \underbrace{4\left(\Delta\phi_{t,1} - \Delta\phi_{t,2}\right)}_{\text{tapers}}, \tag{5}$$

where $\Delta\phi_t$ is the taper-induced phase. In order to retain the fabrication-tolerant performance of this MZI, we need to eliminate the second term of (5). Fig. 6(b) shows the taper-induced phase as a function of taper length for three different output widths. The output widths correspond to the waveguide width of each MZI arm. We can choose an arbitrary phase value $\Delta\theta$ and determine the points where it intersects with the phase plots for
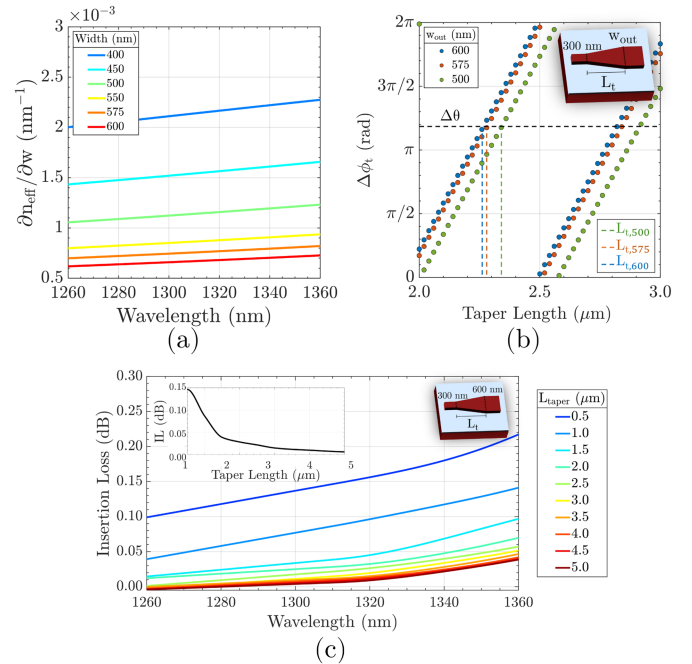

Fig. 6. Simulations results for (a) Partial derivative of the effective index with respect to waveguide width change as a function of wavelength for various waveguide widths; (b) Total accumulated phase of a linear taper for various output widths as a function of taper length for $\lambda = 1310$ nm. The black dashed line dictates the corresponding lengths of each output width that contribute identical phase-shift, which are traced through the colored dashed lines; and (c) IL of a linear taper converting a waveguide of 300 nm width to 600 nm width as a function of wavelength for various taper lengths. The inset figure shows the IL as a function of taper length at 1310 nm wavelength.

each output taper width. Thus, we obtain the corresponding taper lengths such that $\angle L_{t,500} \simeq \angle L_{t,575} \simeq \angle L_{t,600}$, thereby minimizing the second term of (5) when choosing any combination of 2 from these 3 widths for the MZI. Even though these lengths guarantee phase balance, they are not fabrication-tolerant themselves. This means that in the case of waveguide width offset due to fabrication error, the phases of the two tapers will no longer be balanced. Thus, we aim to use short tapers in order to minimize this potential fabrication-induced phase offset. However, we cannot use arbitrarily short tapers, as shorter tapers have increased IL. Fig. 6(c) shows the IL of a $300 \to 600$ taper as a function of wavelength for various taper lengths. The IL appears to converge for longer tapers. The inset figure shows the IL as a function of taper length for $\lambda = 1310$ nm, which shows that the convergence begins after $L_t = 2\,\mu\text{m}$. In order to compromise between acceptable potential phase error and low IL we define the taper lengths as $L_{t,500} = 2.345\,\mu\text{m}$, $L_{t,575} = 2.285\,\mu\text{m}$, and $L_{t,600} = 2.27\,\mu\text{m}$. The phase and IL measurements for the linear tapers were performed using 3D-FDTD simulations.

Lastly, we demonstrate the validity of the assumptions described above in Fig. 7(a) and (b), which shows the effect of a ± 10 nm width offset on a specific WDM channel. This width offset was chosen as it resembles the platform's lithography margin [32]. As expected, in the case of standard MZI-based WDM (blue color in Fig. 7), the output channel position shows a very large spectral shift (13.6 nm).
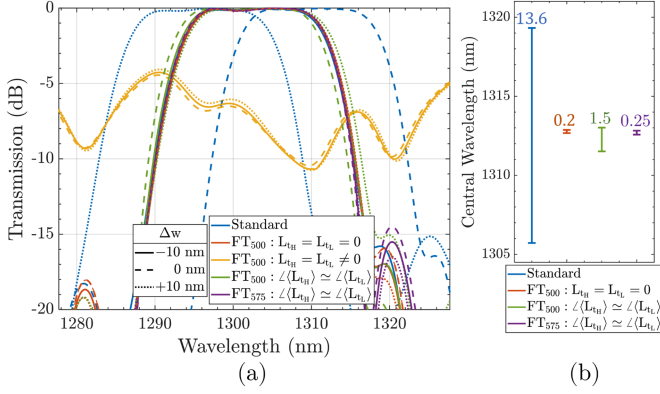
Fig. 7. Effect of waveguide width offset on WDM performance: (a) Channel 2 spectrum for different MZI configurations showing the effect of different waveguide widths (±10 nm). Standard MZI configuration (blue) exhibits a large spectral shift, while it is minimized when we consider an FT_{500} design (red), which is hypothetical due to the absence of tapers. Including tapers of equal length for each arm causes the channel performance to completely break down (yellow), however when the tapers are phase-balanced (green) the spectral shift is satisfactory. Moreover, implementing the FT_{575} configuration (purple) decreases the spectral shift even further; (b) Total spectral shift of each aforementioned configuration for a ±10 nm waveguide width range.

For each FT configuration, the highest waveguide width is fixed as 600 nm, while the lower waveguide width will be either 500 or 575 nm depending on the configuration. Henceforth, these two configurations will be denoted as FT_{500} and FT_{575}, respectively. The lowest spectral shift (0.2 nm) is observed for an FT_{500} when we consider a hypothetical case by neglecting the effect of the tapers (orange color in Fig. 7), i.e. $L_{t_H} = L_{t_L} = 0$, where subscripts H and L correspond to high and low width, respectively, thus satisfying (4a). We observe that when we include tapers of equal length ($L_{t_H} = L_{t_L} \neq 0$) the channel shape completely breaks down (yellow color in Fig. 7). This is expected, as each taper will induce different phase shifts per arm, which will cause a phase error that will propagate and accumulate throughout the WDM structure. For an FT_{500} configuration, when the taper lengths are defined based on Fig. 6(b), the channel shape is retained (green color in Fig. 7). As previously discussed, the tapers themselves are not fabrication-tolerant, thus the spectral shift, in this case, is increased to 1.5 nm. We can reduce the spectral shift even further by choosing widths that have more similar values, i.e., $w_L = 575$ and $w_H = 600$ nm. In this case, the waveguide width offset of ±10 nm will induce a smaller phase difference between the two tapers, because their lengths and output widths are more similar to each other (Fig. 6(b)), compared to the case where $w_L = 500$ and $w_H = 600$ nm. We can observe this for the FT_{575} configuration (purple color in Fig. 7), where the spectral shift is reduced to 0.25 nm. To conclude, w_L, and w_H can be chosen freely, with large values being more desirable due to increased insensitivity to dimension variations. As $|w_L - w_H|$ is decreased, the spectral shift is decreased as well, however, the device footprint becomes larger. Subsequently, as the difference between the two waveguide widths increases, the device becomes more compact, while exhibiting a larger spectral shift.

C. Cascaded MZI Lattice

In this section, the WDM operation will be briefly discussed. The design aimed for a 4-channel filter, with a channel spacing of 20 nm. A block diagram of the device can be seen in Fig. 8(a), where the routing of each signal is denoted. It consists of two types of stages called S_1 and S_2 which consist of 3 and 2 MZIs, respectively. Stage S_1 separates the 4 channels in pairs λ_1, λ_3, and λ_2, λ_4, while S_{1A} and S_{1B} contribute towards flattening the channel response as well as decreasing the channel crosstalk. Subsequently, stages S_{2A} and S_{2B}, which operate with half the FSR of the S_1 stages, split the channel pairs to individual channels, while S_{2A1}, S_{2A2}, S_{2B1}, and S_{2B2} further contribute to channel flatness and decreased crosstalk. The entire lattice consists of 3 grouped stages with suffixes S_1, S_{2A}, and S_{2B}. Each of these groups contains 3 individual stages which are identical. In principle, we can achieve WDM operation just by including the stages S_1, S_{2A}, and S_{2B} as shown in [16]. However, implementing an additional duplicate of each stage helps to further decrease the crosstalk and increase channel flatness, similar to a high-order ring resonator-based WDM system [44]. Fig. 8(b) shows a zoomed-in view of S_1 with the corresponding WIC SRs, and phase induced by each MZI arm. The phase difference between the two arms of each MZI follows the rules set by [16]. The phase terms denoted at each of the MZI arms include the phase induced by propagation along the waveguide (βL), the tapers ($\Delta\phi_t$), and the required additional length to compensate for the excess phase ($\Delta\phi_{WIC}$) added by the aforementioned WIC as described in Section II-A. Fig. 8(c) shows a top view of the WDM filter depicting the corresponding SRs of each WIC denoted. The black rectangles in Fig. 8(a), (c) represent optical absorbers to eliminate potential residues from neighboring channels. An optical absorber is essentially an optical terminator, i.e., a device that absorbs and terminates incoming light, reducing unwanted back-reflections.

III. EXPERIMENTAL RESULTS

In order to validate our assumptions, we have fabricated two WDM configurations, each one with a different set of waveguide widths. More specifically, we fabricated the two configurations mentioned in Section II-B, FT_{500} and FT_{575} in order to investigate the trade-off between device footprint and spectral shift. The measurements were conducted by a fully automated wafer-level photonic device testing setup [45].

A. Taper and Bend Insertion Loss

Before we assess the performance of the WDM filters, we examine the IL of the discrete fundamental components that include the linear tapers and the circular bends which are a part of the WICs and the routing waveguides. To obtain the IL, we measured the optical power obtained from a different number of cascaded components as well as a reference waveguide with a configuration that is visualized schematically in Fig. 9(a). More specifically, we measured the power of 80, 160, and 240 ($M = 80$) cascaded 90° bends and plot the optical power spectra for all the aforementioned number of cascaded components as
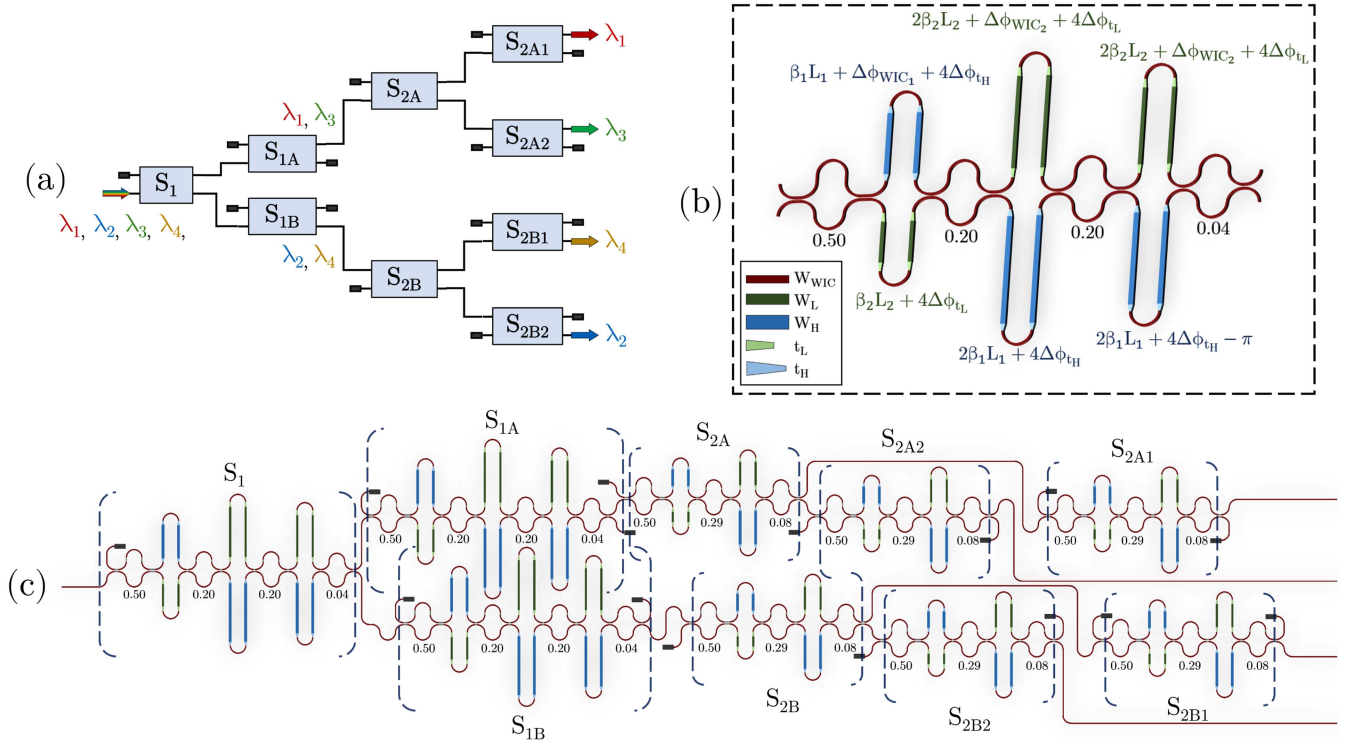
Fig. 8.   WDM filter configuration: (a) Top view schematic of the cascaded MZI lattice with each individual stage and the corresponding WIC SRs denoted; (b) Zoomed-in illustration of Stage 1 (S_1) depicting the phase induced by every component on each MZI arm, as well as the SR of each WIC; and (c) block diagram of the WDM filter demonstrating the routing of the initial multiplexed pulse until it is fully de-multiplexed. The black rectangles represent optical absorbers.
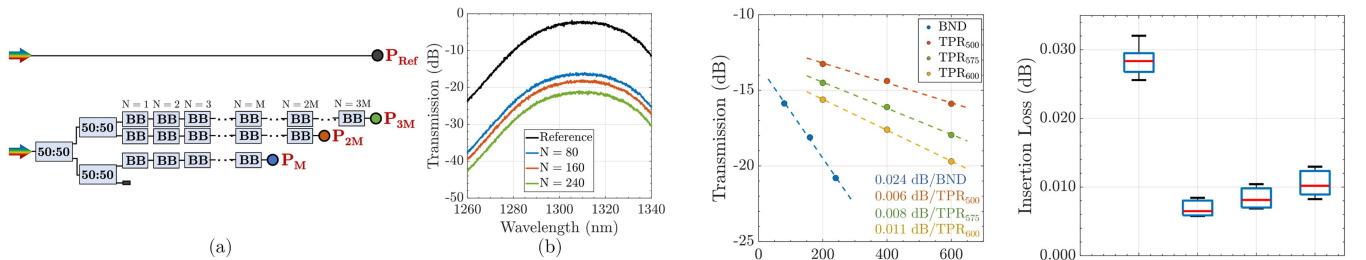

Fig. 9.   Insertion loss extraction configuration. (a) Schematic of different numbers of cascaded components and reference waveguide for normalization. For the 90° bend, M = 80, while for the tapers M = 200; (b) Normalized transmission spectra for the reference waveguide, and for the three lines of different numbers of cascaded 90° bends. The color of each curve corresponds to the output color of each line in 9(a).

shown in Fig. 9(b). As expected, insertion loss is increased as the number of cascaded components is increased. We can use the three obtained transmission values ($N = 80, 160, 240$) for each wavelength. Each of these points expresses the accumulated IL for a specific number of components, thus the IL per each quarter bend can be obtained by the slope of the lines shown in Fig. 10(a). This particular graph corresponds to $\lambda = 1310$ nm, but we can generalize this to every wavelength as will be shown subsequently.

We then applied the same principle to obtain the IL of each taper as well, for which the number of devices was 200, 400, and 600 respectively, i.e., $M = 200$. Fig. 10(b) shows the statistical results for 5 different wafer sites at $\lambda = 1310$ nm. Tapers
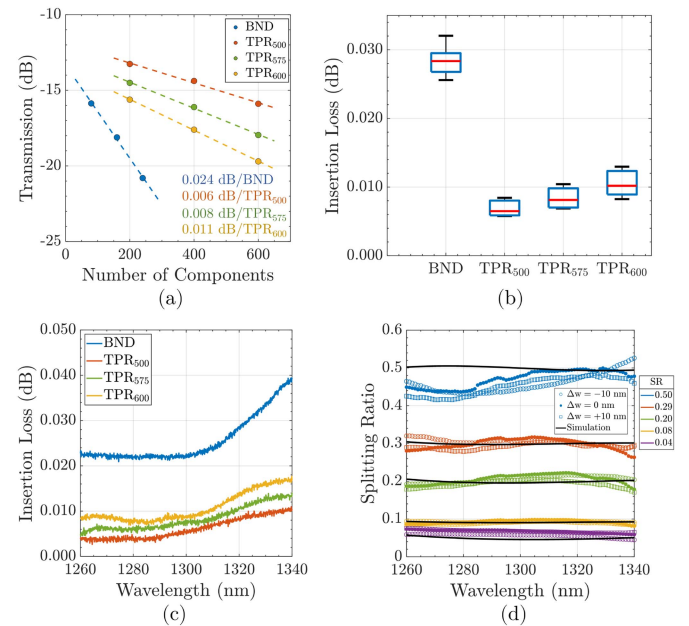

Fig. 10.   Hardware response for the building blocks: (a) Optical power transmission measurements for each of the four components with respect to a total number of cascaded components for $\lambda = 1310$ nm. Inset values denote the slopes of each component; (b) Statistical IL analysis for each component at $\lambda = 1310$ nm. The red line denotes the median value, while the blue box corresponds to the range between the 25th and 75th percentile; (c) Experimental IL spectra for each component; and (d) experimental spectra of the 5 fabricated WICs. The results of each design demonstrate the inherent fabrication tolerance characteristics by showing consistent performance for a waveguide width offset of ± 10 nm. The black lines indicate the simulated SR for each coupler as shown in Fig. 5(a).
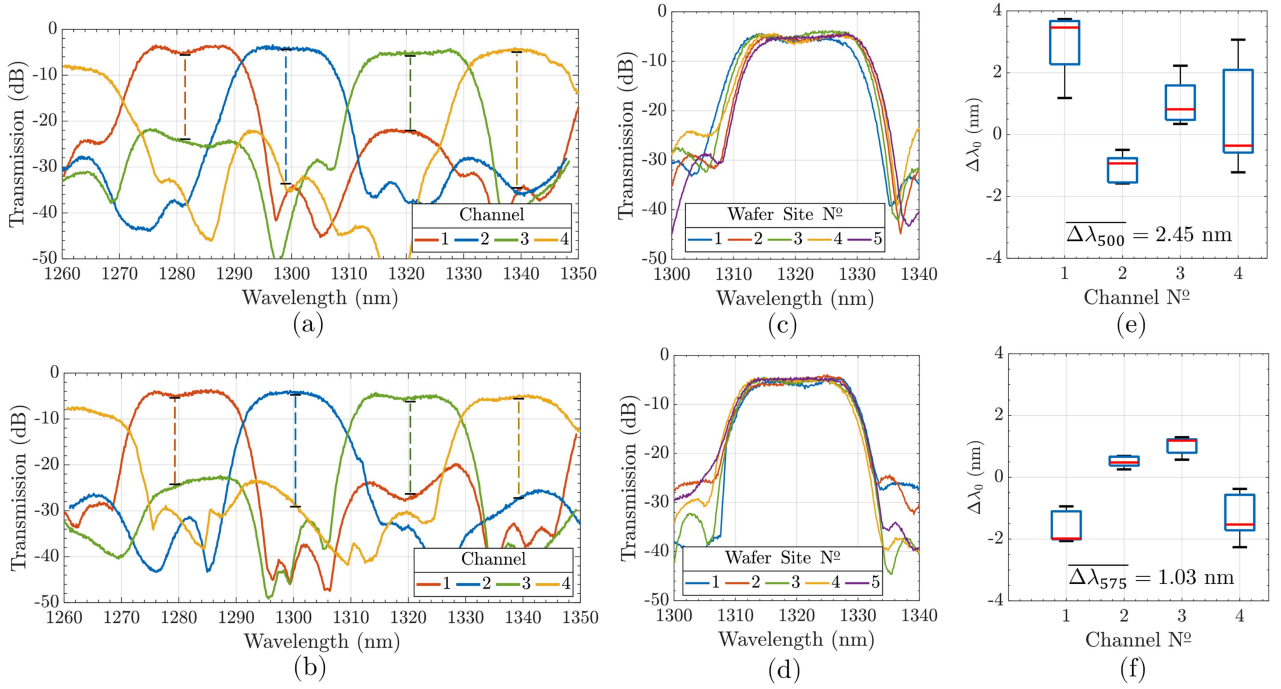
Fig. 11. WDM filter spectra of the first wafer site for the (a) FT_{500}, and (b) FT_{575} configurations. The dashed lines indicate the induced crosstalk for each channel; Channel 3 performance for 5 different wafer sites for the (c) FT_{500}, and (d) FT_{575} configurations; Statistical results for the spectral shift of each WDM channel for the (e) FT_{500}, and (f) FT_{575} configurations. The y-axis indicates the spectral offset with respect to the intended wavelength centers λ_0 of each channel, i.e., 1280, 1300, 1320, and 1340 nm. Each figure contains the mean spectral deviation of each channel, indicating that the FT_{575} device is $\sim$1.9 times more fabrication-tolerant compared to the FT_{500} device.

with larger output width demonstrate higher IL which can be attributed to lower taper length and higher output width as well as larger width difference compared to the input taper width of 300 nm. Additionally, Fig. 10(c) shows the IL with respect to wavelength, where each wavelength point corresponds to a different slope (Fig. 10(a)). We notice that the IL is increased for longer wavelengths which can be attributed to the weaker modal confinement [40]. Furthermore, we characterized the performance of the WICs. Each design was fabricated with an intentional width offset of ±10 nm, in order to test the robustness of the approach shown in Fig. 5(a). The results are visualized in Fig. 10(d). Each design shows excellent performance stability, with an increased performance deviation for longer DCs. This occurs due to the deviation of the total accumulated phase between the three cases, which will be higher as the DC length is increased. Moreover, it is observed that the WIC aiming at SR = 0.5 demonstrates an apparent deviation from the intended SR, especially for shorter wavelengths. This deviation led to increased channel crosstalk, which will be analyzed in the following section.

B. WDM Filter Performance

In this section, the WDM filter results for each configuration will be presented. Fig. 11(a) and (b) show the de-multiplexed spectra of each channel for the FT_{500}, and FT_{575} filters. We can see that both devices perform well, albeit with increased crosstalk compared to the one we expect theoretically [46]. The most probable justification behind the increased crosstalk

is the deviation of the 3-dB WIC. The 3-dB power splitting theoretically enables total destructive interference of λ_2, and λ_4 on the S_{2A} segment (Fig. 8(c)), as well as λ_1, and λ_3 on the S_{2B} segment. However, due to the SR deviation, we cannot achieve total destructive interference, thus generating channel crosstalk, which is also amplified by potential phase errors caused by imperfectly defined taper widths. Additionally, this implies that a larger ratio of the input power for a specific wavelength, e.g. λ_1 will route towards channels 2, 3, and 4, thus reducing the total received power in channel 1, which will lead to excess IL added to the unavoidable IL caused by the components presented in Fig. 10. This figure suggests that the dominant IL factor is the large number of sharp bends located in the WIC.

Fig. 11(c) and (d) show the spectra of channel 3 for 5 different wafer sites. We observe consistent performance for both devices, however, it is apparent that FT_{575} offers superior fabrication tolerance, as predicted theoretically by Fig. 7. This performance is quantified for both devices and all channels in Fig. 11(e) and (f). These figures express the statistical distribution of each channel's central wavelength with respect to the originally intended center wavelengths, i.e. $\lambda_1 = 1280$ nm, $\lambda_2 = 1340$ nm, $\lambda_3 = 1300$ nm, and $\lambda_4 = 1320$ nm ($\Delta\lambda_0 = 0$). This was designed intentionally different from the International Telecommunication Union (ITU)-recommended wavelength peaks [47] based on a specific application. The channel spacing itself is ITU-recommended at $\Delta\lambda = 20$ nm. However, both the channel spacing and the peaks' positions can easily be tuned by the proposed model through the interference condition of the MZIs (4) without loss of generality. The obtained results show

that FT_{575} offers higher fabrication tolerance for every channel compared to FT_{500} as expected by theory, with a mean total spectral shift of 1.03 nm and 2.45 nm, respectively. Moreover, FT_{575} outperforms FT_{500} in terms of total spectral shift and crosstalk. However, as mentioned in Section II-B, (4a), FT_{575} has a larger footprint by a factor of 1.9. Specifically, the FT_{575} and FT_{500} designs have footprints of 0.582 mm^2 and 0.305 mm^2, respectively. Thus, we confirm that there is a trade-off between device footprint and fabrication tolerance, as derived from our numerical model presented in Section II. Moreover, the total device footprint for either configuration is significantly lower compared to similar multiple-stage MZI-based cWDM configurations [17], [27] reported in the literature, due to optimized architecture between the different WDM stages (Fig. 8(a)).

Regarding the IL, we can quantify it by summing the total amount of 90° bends and tapers and multiplying by the respective IL as presented in Fig. 10(a). We can approximate the total loss for the channel located at $\lambda = 1300$ nm as:

$$IL_{1300} \simeq 104 \times IL_{90°} + 16 \times IL_{TPR_H} + 24 \times IL_{TPR_L}$$

$$\simeq \underbrace{2.45}_{90° \text{ bend}} + \underbrace{0.13}_{w_H \text{ taper}} + \underbrace{0.14}_{w_L \text{ taper}} = \underbrace{2.72\,\text{dB}}_{IL_{1300}}. \qquad (6)$$

Equation (6) shows that the main contributing IL factor are the sharp bends present in the WICs. The excess loss, compared to the obtained result that is shown in Fig. 11, can be attributed to the additional bends used for the channel routing and to propagation loss.

Table I shows a comparison of the relevant figures of merit between this work and the state-of-the-art. We can see that our device offers the second-lowest spectral shift, albeit with a significantly lower footprint. As predicted by theory in Fig. 7 and shown experimentally in Fig. 11, we can achieve an even lower spectral shift by choosing a larger w_L value. Regarding the insertion loss and crosstalk, the main limiting factor is the spectrum generated by the 50:50 WIC and the wavelength-dependent insertion loss of every WIC. A WIC based on Bézier bends was recently presented [50], that experimentally demonstrates lower and spectrally stable insertion loss, a footprint reduction by a factor of 20 times, and consistent 50:50 SR compared to the WIC used in this work. Implementing this power splitter in the WDM filter can greatly improve the total device IL, and crosstalk, but also reduce the total footprint of the device.

IV. CONCLUSION

We designed, simulated, and experimentally demonstrated fabrication-tolerant WDM filters based on Mach-Zehnder Interferometers using wavelength-independent power splitters. The devices are realized on a state-of-the-art CMOS-compatible monolithic silicon photonics platform, which enables direct implementation with on-chip electronics and silicon/silicon nitride photonics for optimized integration density. The fabrication insensitivity of the devices was achieved by including broadband robust power splitters, and MZIs consisting of arms of different widths. Phase-balanced linear tapers of different lengths were introduced in order to achieve fabrication-tolerant performance which allowed us to choose any waveguide width for each of the

MZI arms. To ensure performance consistency, we tested two WDM configurations consisting of different MZI arm widths across various wafer sites. Experimental characterization of the devices demonstrated excellent fabrication-tolerant performance, which revealed an inherent trade-off between device footprint and channel spectral shift. More specifically, the two configurations demonstrated mean maximum spectral shifts of 1.03 nm, and 2.45 nm, with a total footprint of 0.582 mm^2, and 0.305 mm^2, respectively. The IL loss and crosstalk of the device can be further optimized by including 3-dB splitters consisting of adiabatic Bézier bends, which can offer reduced footprint, minimized IL and crosstalk, and high spectral stability.

REFERENCES

[1] S. Park, K. J. Kim, I. G. Kim, and G. Kim, "Si micro-ring MUX/DeMUX WDM filters," *Opt. Exp.*, vol. 19, no. 14, pp. 13531–13539, 2011.

[2] M. S. Dahlem, C. W. Holzwarth, A. Khilo, F. X. Kärtner, H. I. Smith, and E. P. Ippen, "Reconfigurable multi-channel second-order silicon microring-resonator filterbanks for on-chip WDM systems," *Opt. Exp.*, vol. 19, no. 1, pp. 306–316, 2011.

[3] D. Dai, P. Chen, S. Chen, X. Guan, and Y. Shi, "High-order microring resonators with bent couplers for a box-like filter response," *Opt. Lett.*, vol. 39, no. 21, pp. 6304–6307, 2014.

[4] T. Fukazawa, F. Ohno, and T. Baba, "Very compact arrayed-waveguide-grating demultiplexer using Si photonic wire waveguides," *Japanese J. Appl. Phys.*, vol. 43, no. 5B, pp. L673–L675, 2004.

[5] S. Pathak, M. Vanslembrouck, P. Dumon, D. V. Thourhout, and W. Bogaerts, "Optimized silicon AWG with flattened spectral response using an MMI aperture," *J. Lightw. Technol.*, vol. 31, no. 1, pp. 87–93, Jan. 2013.

[6] A. Taha et al., "Compact MMI-Based AWGs in a scalable monolithic silicon photonics platform," *IEEE Photon. J.*, vol. 13, no. 4, Aug. 2021, Art. no. 6600306.

[7] F. Horst, W. M. J. Green, B. J. Offrein, and Y. A. Vlasov, "Silicon-on-insulator echelle grating WDM demultiplexers with two stigmatic points," *IEEE Photon. Technol. Lett.*, vol. 21, no. 23, pp. 1743–1745, Dec. 2009.

[8] D. Feng et al., "Fabrication insensitive echelle grating in silicon-on-insulator platform," *IEEE Photon. Technol. Lett.*, vol. 23, no. 5, pp. 284–286, Mar. 2011.

[9] D. Melati et al., "Compact and low crosstalk echelle grating demultiplexer on silicon-on-insulator technology," *Electronics*, vol. 8, no. 6, 2019, Art. no. 687.

[10] C. Lin et al., "Ultra-compact, flat-top demultiplexer using anti-reflection contra-directional couplers for CWDM networks on silicon," *Opt. Exp.*, vol. 21, no. 6, pp. 6733–6738, 2013.

[11] H. Yun, M. Hammood, L. Chrostowski, and N. A. F. Jaeger, "Optical add-drop filters using cladding-modulated sub-wavelength grating contra-directional couplers for silicon-on-insulator platforms," in *Proc. IEEE Int. Conf. Electron. Mobile Commun.*, 2019, pp. 0926–0931.

[12] H. Yun, L. Chrostowski, M. Hammood, N. A. F. Jaeger, and S. Lin, "Broadband flat-top SOI add–drop filters using apodized sub-wavelength grating contradirectional couplers," *Opt. Lett.*, vol. 44, no. 20, pp. 4929–4932, 2019.

[13] Y. Gebregiorgis et al., "Apodized distributed Bragg reflector (DBR) bends for compact cWDM filter," in *Proc. OSA Adv. Photon. Congr.*, Washington, DC, USA, 2021, Paper IM1B.5.

[14] Y. Gebregiorgis et al., "Straight and curved distributed Bragg reflector design for compact WDM filters," *Opt. Exp.*, vol. 31, no. 7, pp. 11519–11535, 2023.

[15] K. Jinguji and M. Oguma, "Optical half-band filters," *J. Lightw. Technol.*, vol. 18, no. 2, pp. 252–259, Feb. 2000.

[16] F. Horst, W. M. J. Green, S. Assefa, S. M. Shank, Y. A. Vlasov, and B. J. Offrein, "Cascaded Mach-Zehnder wavelength filters in silicon photonics for low loss and flat pass-band WDM (de-)multiplexing," *Opt. Exp.*, vol. 21, no. 10, pp. 11652–11658, 2013.

[17] A. Bois, D. Mahgerefteh, J. C. Mikkelsen, J. K. S. Poon, S. Menezo, and T. Lordello, "Polarization-insensitive silicon nitride Mach-Zehnder lattice wavelength demultiplexers for CWDM in the O-band," *Opt. Exp.*, vol. 26, no. 23, pp. 30076–30084, 2018.

[18] H. Xu and Y. Shi, "Flat-top CWDM (De)Multiplexer based on MZI with bent directional couplers," *IEEE Photon. Technol. Lett.*, vol. 30, no. 2, pp. 169–172, Jan. 2018.

[19] Z. Lu et al., "Performance prediction for silicon photonics integrated circuits with layout-dependent correlated manufacturing variability," *Opt. Exp.*, vol. 25, no. 9, pp. 9712–9733, 2017.

[20] N. M. Ravindra and V.K. Srivastava, "Temperature dependence of the energy gap in semiconductors," *J. Phys. Chem. Solids*, vol. 40, no. 10, pp. 791–793, 1979.

[21] S. Dwivedi, H. D'heer, and W. Bogaerts, "Fabrication tolerant silicon MZI filter," in *Proc. IEEE Int. Conf. Group IV Photon.*, 2014, pp. 147–148.

[22] B. Guha, A. Gondarenko, and M. Lipson, "Minimizing temperature sensitivity of silicon Mach-Zehnder interferometers," *Opt. Exp.*, vol. 18, no. 3, pp. 1879–1887, 2010.

[23] P. Xing and J. Viegas, "Broadband CMOS-compatible SOI temperature insensitive Mach-Zehnder interferometer," *Opt. Exp.*, vol. 23, no. 19, pp. 24098–24107, 2015.

[24] G. Gao et al., "Silicon nitride O-band (de)multiplexers with low thermal sensitivity," *Opt. Exp.*, vol. 25, no. 11, pp. 12260–12267, 2017.

[25] Y. Gebregiorgis et al., "Thermo-optic phase shifter for photonic neural networks," in *Proc. Front. Opt.*, Rochester, NY, USA, 2022, Paper JW5A.99.

[26] S.-H. Jeong and Y. Tanaka, "Silicon-wire optical demultiplexers based on multistage delayed Mach-Zehnder interferometers for higher production yield," *Appl. Opt.*, vol. 57, no. 22, pp. 6474–6480, 2018.

[27] T. H. Yen and Y. J. Hung, "Fabrication-tolerant CWDM (de)Multiplexer based on cascaded Mach-Zehnder interferometers on silicon-on-insulator," *J. Lightw. Technol.*, vol. 39, no. 1, pp. 146–153, Jan. 2021.

[28] A. Yariv, "Coupled-mode theory for guided-wave optics," *IEEE J. Quantum Electron.*, vol. 9, no. 9, pp. 919–933, Sep. 1973.

[29] W. Huang, "Coupled-mode theory for optical waveguides: An overview," *JOSA A*, vol. 11, no. 3, pp. 963–983, 1994.

[30] H. Yamada, T. Chu, S. Ishida, and Y. Arakawa, "Optical directional coupler based on Si-wire waveguides," *IEEE Photon. Technol. Lett.*, vol. 17, no. 3, pp. 585–587, Mar. 2005.

[31] M. Papadovasilakis et al., "Low-loss 2 × 2 wavelength-independent coupler using MZI based on bézier curves," in *Proc. Front. Optics*, Washington, DC, USA, 2021, Paper JW7A.135.

[32] K. Giewont et al., "300-mm monolithic silicon photonics foundry technology," *IEEE J. Sel. Topics Quantum Electron.*, vol. 25, no. 5, pp. 1–11, Sep./Oct. 2019.

[33] M. Rakowski et al., "45nm CMOS-silicon photonics monolithic technology (45CLO) for next-generation, low power and high speed optical interconnects," in *Proc. Opt. Fiber Commun. Conf.*, Washington, DC, USA, 2020, Paper T3H.3.

[34] Y. Bian et al., "Towards low-loss monolithic silicon and nitride photonic building blocks in state-of-the-art 300 mm CMOS foundry," in *Proc. Front. Optics*, Washington, DC, USA, 2020, Paper FW5D.2.

[35] Y. Bian et al., "Monolithically integrated silicon nitride platform," in *Proc. Opt. Fiber Commun. Conf.*, Washington, DC, USA, 2021, vol. 46, Paper Th1A.

[36] S. Chandran et al., "Beam shaping for ultra-compact waveguide crossings on monolithic silicon photonics platform," *Opt. Lett.*, vol. 45, no. 22, pp. 6230–6233, 2020.

[37] Y. Bian et al., "Wavelength-division multiplexing filters including assisted coupling regions," 2023, 100.

[38] B. E. Little and T. Murphy, "Design rules for maximally flat wavelength-insensitive optical power dividers using mach-zehnder structures," *IEEE Photon. Technol. Lett.*, vol. 9, no. 12, pp. 1607–1609, Dec. 1997.

[39] Y. Bian et al., "3D integrated laser attach technology on a 300-mm monolithic CMOS silicon photonics platform," *IEEE J. Sel. Topics Quantum Electron.*, vol. 29, no. 3, pp. 1–19, May/Jun. 2023.

[40] M. Papadovasilakis et al., "Fabrication tolerant and wavelength independent arbitrary power splitters on a monolithic silicon photonics platform," *Opt. Exp.*, vol. 30, no. 19, pp. 33780–33791, 2022.

[41] T. Horikawa et al., "A 300-mm silicon photonics platform for large-scale device integration," *IEEE J. Sel. Top. Quantum Electron.*, vol. 24, no. 4, pp. 1–15, Jul./Aug. 2018.

[42] C. K. Madsen and J. H. Zhao, *Optical Filter Design and Analysis: A. Signal Processing Approach*. Hoboken, NJ, USA: Wiley, 1999.

[43] L. Chrostowski and M. Hochberg, *Silicon Photonics Design: From Devices to Systems*. Cambridge, U.K.: Cambridge Univ. Press, 2015.

[44] F. Xia, M. Rooks, L. Sekaric, and Y. Vlasov, "Ultra-compact high order ring resonator filters using submicron silicon photonic wires for on-chip optical interconnects," *Opt. Exp.*, vol. 15, no. 19, no. 19, pp. 11934–11941, 2007.

[45] A. Aboketaf et al., "Towards fully automated testing and characterization for photonic compact modeling on 300-mm wafer platform," in *Proc. Opt. Fiber Commun. Conf.*, Washington, DC, USA, 2021, Paper W6A.1.

[46] M. Papadovasilakis et al., "Fabrication tolerant MZI design for broadband WDM filters on scalable SiP platform," in *Proc. OSA Adv. Photon. Congr.*, Washington, DC, USA, 2021, Paper IM2A.6.

[47] M. Joncic, M. Haupt, and U. H. P. Fischer, "Investigation on spectral grids for VIS WDM applications over SIPOF," in *Proc. IEEE ITG Symp. Photon. Netw.*, 2013, pp. 1–6.

[48] J. R. Ong, T. X. Guo, T. Y. Ang, S. T. Lim, H. Wang, and C. E. Png, "Wafer-level characterization of silicon nitride CWDM (de) multiplexers using Bayesian inference," *IEEE Photon. Technol. Lett.*, vol. 32, no. 15, pp. 917–920, Aug. 2020.

[49] J. Y. Lee, T. Ling, R. S. Tummidi, M. Webster, and P. Gothoskar, "Fabrication-tolerant nitride lattice filter for CWDM," in *Proc. Opt. Fiber Commun. Conf.*, Washington, DC, USA, 2021, Paper Tu5B.2.

[50] M. Papadovasilakis et al., "Compact, broadband, and low-loss power splitters using MZI based on bézier bends," *Opt. Exp.*, vol. 31, no. 6, pp. 10862–10875, 2023.